JACS
JOURNAL OF THE AMERICAN CHEMICAL SOCIETY
pubs.acs.org/JACS

Article

Exciton Delocalization Promotes Far-Red Absorption in a Tetrameric Chlorophyll *a* Light-Harvesting Complex from *Trachydiscus minutus*

Soichiro Seki,* Lorenzo Cupellini, David Bína, Elena Betti, Petra Urajová, Hideaki Tanaka, Tomoko Miyata, Keiichi Namba, Genji Kurisu, Tomáš Polívka, Radek Litvín,* and Ritsuko Fujii*

Cite This: *J. Am. Chem. Soc.* 2025, 147, 47675−47689

Read Online

ACCESS | Metrics & More | Article Recommendations | Supporting Information

ABSTRACT: Photosynthetic organisms employ light-harvesting complexes (LHCs) to optimize energy capture under variable light conditions. The freshwater eustigmatophyte *Trachydiscus minutus* accumulates a red-shifted violaxanthin−chlorophyll protein (rVCP) that contributes to far-red light harvesting using only chlorophyll (Chl) *a* molecules, without chemical modification or substitution of pigments. Based on high-resolution cryo-EM and multiscale quantum chemical calculations, we uncovered a heterodimer-based tetrameric architecture, representing a unique oligomerization mode among LHCs. Within each heterodimer, Chls *a* are distinctively arranged adjacent to the terminal emitter, forming an unprecedentedly extended chlorophyll cluster. Quantum chemical calculations reveal three strong exciton-coupled pigment domains, two of which reside in the large cluster and solely account for the intense far-red absorption near 700 nm without contributions from charge−transfer states. Our structural and quantum chemical characterizations of far-red light harvesting reveal a molecular mechanism of red spectral tuning that relies on protein-controlled excitonic coupling of identical Chl *a* pigments, as demonstrated here in this eustigmatophyte, highlighting diverse adaptations for harvesting spectrally shifted, low-energy light.

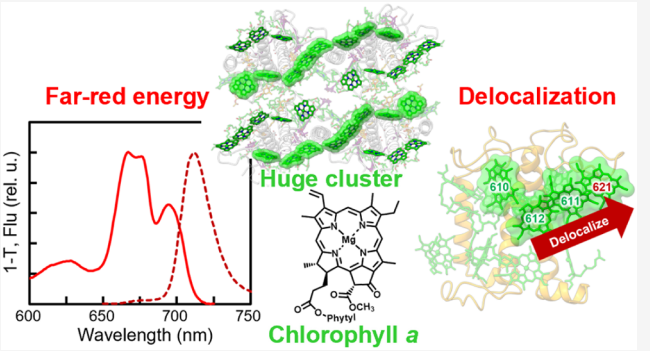

INTRODUCTION

Oxygenic photosynthesis powers life on Earth by converting light to chemical energy. In both natural and cultivated ecosystems, photosynthetic organisms often inhabit stratified environments where overlying vegetation or water filters incoming light, reducing its intensity and altering its spectral composition. Given the sparse and fluctuating availability of sunlight at the molecular scale—particularly in such shaded conditions—photosynthetic eukaryotes depend on light-harvesting complexes (LHCs), which concentrate energy through proteins binding chlorophyll *a* (Chl *a*) and accessory pigments.[1−4]

However, light suitable for the excitation of Chl *a* and its common accessory pigments penetrates only a few foliage layers or several decimeters into eutrophic water.[5] To compensate, some organisms have evolved the ability to harvest far-red light, which is less utilized by competitors. Cyanobacteria, for instance, can synthesize far-red-absorbing Chl *d* and Chl *f*.[6,7] In plants, photosystem II (PSII) preferentially accepts shorter wavelengths, aided by Chl *b*, while photosystem I (PSI) extends into the far-red region using exclusively Chl *a* within LHCI.[8] Certain stramenopile algae possess light-harvesting complexes that achieve far-red absorption using only Chl *a* without employing any modified forms of chlorophyll. Unlike plant systems, stramenopiles lack strong spectral separation between PSII and PSI, and their far-red antennae transfer excitation energy to PSII.[9,10]

Spectral tuning of light absorption in photosynthetic antennas represents a promising strategy for enhancing the productivity of vertically structured crops, agroforestry systems, and dense algal cultures in biotechnological facilities.[11−13] These production systems often suffer from limited light availability in the lower canopy layers, which constrains photosynthetic efficiency and reduces the overall yield. Therefore, understanding the diverse mechanisms of far-red light absorption is crucial for enabling the intentional manipulation of crop light absorption spectra.

The spectral characteristics of LHCs arise not only from the pigments themselves but also from their interactions with surrounding proteins and neighboring pigments. For instance, the red-shifted absorption of Chl *a* at 690−700 nm in plant LHCI has been attributed to strong excitonic coupling combined with charge−transfer state mixing between two

Received: October 1, 2025
Revised: December 1, 2025
Accepted: December 2, 2025
Published: December 13, 2025

https://doi.org/10.1021/jacs.5c17299
J. Am. Chem. Soc. 2025, 147, 47675−47689

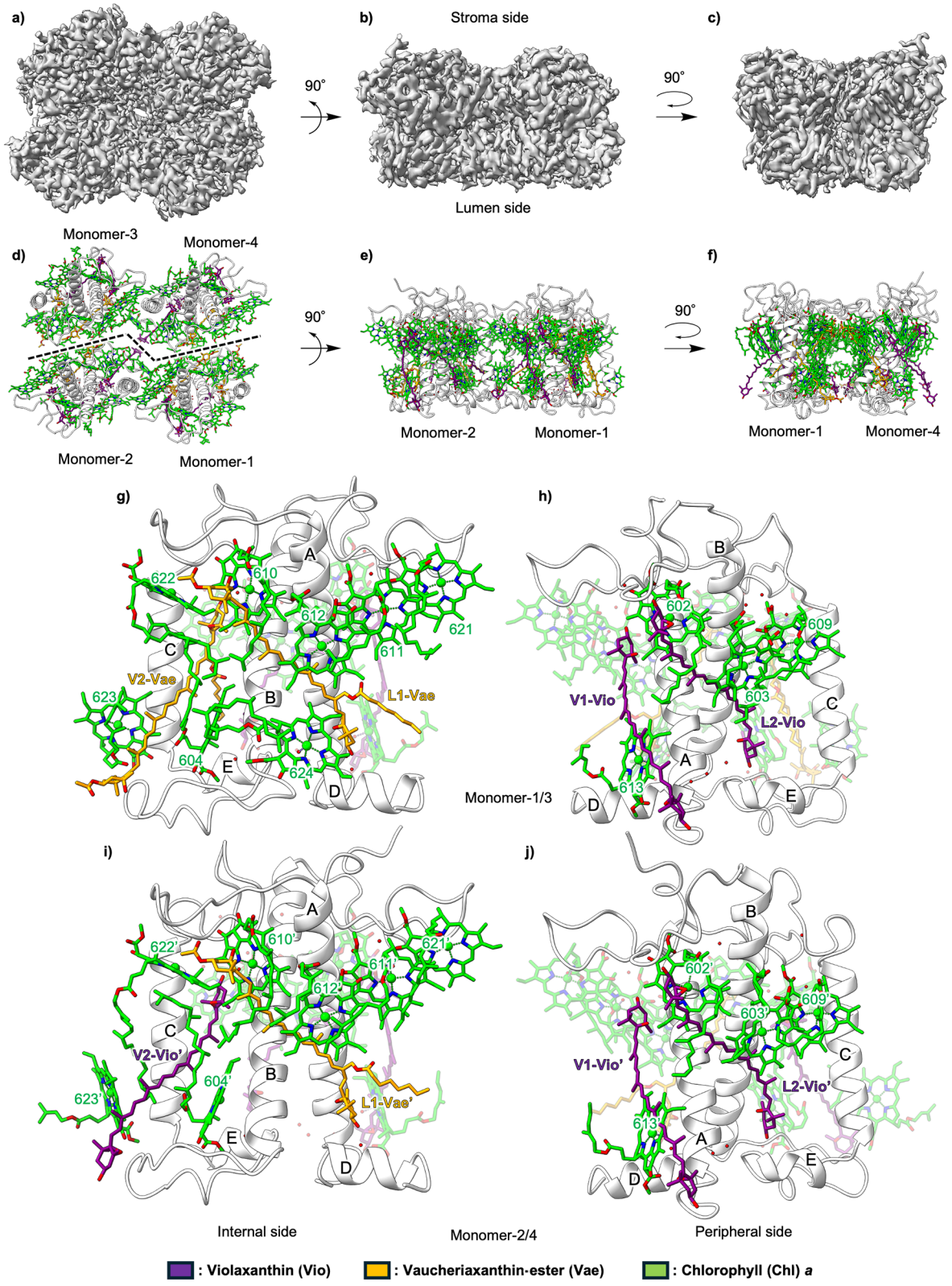

Figure 1. Cryo-EM maps, the corresponding models, and detailed structures of rVCP. Cryo-EM maps (**a**−**c**) and the corresponding models (**d**−**f**) from three different angles are illustrated. Detailed side views of two monomers (monomer-1/3 and monomer-2/4) from the peripheral and internal sides (**g**−**j**) are presented, with color coding as follows: chlorophyll (Chl) *a*, green; vaucheriaxanthin ester (Vae), orange; and violaxanthin (Vio), purple. All maps and models were visualized using ChimeraX.[54]

closely spaced Chl *a* molecules.[14,15] Algal LHCs remain less extensively studied, yet similar mechanisms have recently been proposed in the LHC of the Arctic green alga *Prasiola crispa*,[16] which is not evolutionarily related to plant LHCI.

https://doi.org/10.1021/jacs.5c17299
J. Am. Chem. Soc. 2025, 147, 47675−47689

Eustigmatophytes, although closely related to diatoms, exhibit a distinct light-harvesting strategy. While diatoms rely on Chl *c* and the keto-carotenoid fucoxanthin, eustigmatophytes use only Chl *a* and carotenoids such as violaxanthin and vaucheriaxanthin, which lack conjugated keto groups.[17] Current knowledge of eustigmatophyte light harvesting largely comes from studies of violaxanthin chlorophyll protein (VCP) in *Nannochloropsis oceanica* and red-shifted VCP (rVCP) in *Trachydiscus minutus*. In addition to Raman spectroscopy,[18] ultrafast[19,20] and magnetic resonance[21] techniques have revealed energy-transfer pathways within VCP and rVCP and suggest that excitonic interactions among Chl *a* molecules underlie the red shift near 700 nm observed in rVCP.

Structural insights are essential for validating such mechanisms. High-resolution structures of plant LHCII have been available for over two decades through X-ray crystallography.[22,23] More recently, the high-resolution structure of an algal LHC—a diatom fucoxanthin chlorophyll protein (FCP) dimer—was also resolved by the same method.[24] With the advent of single-particle cryo-electron microscopy (cryo-EM), various FCP supercomplexes in diatoms have since been characterized, revealing diverse oligomeric forms.[25] Modern cryo-EM now reaches sub-2 Å resolution, allowing precise quantum chemical calculations of pigment−pigment interactions and providing mechanistic insights into excited-state dynamics.[26]

Here, we present the cryo-EM structure of the tetrameric far-red antenna complex rVCP from *Trachydiscus minutus*. It features a distinct heterodimer-based tetrameric assembly, which gives rise to a unique spatial arrangement of Chl *a* molecules. With 11.5 Chl *a* per monomer and a Chl/carotenoid ratio of 2.9, its pigment contents and arrangement resemble those of plant LHCII more than those of diatom FCP, highlighting a surprising divergence in the pigment composition from its closer evolutionary relatives. Based on this structure, we performed multiscale quantum chemical calculations to elucidate the molecular origin of far-red absorption. We show that the unique arrangement of Chl *a* molecules in rVCP facilitates a red-shifted absorption through strong exciton delocalization. These findings reveal a previously uncharacterized strategy for red-light harvesting in algae.

RESULTS

Structural Determination and the Whole Structure of rVCP Complex. Prior to structural analysis, we verified that only the highest-order oligomer of rVCP displays characteristic red-shifted absorption, fluorescence, and circular dichroism (CD) signals. The sample used in this study corresponds to fraction B5 from our previous report,[10] whereas lower-order oligomers, such as the putative monomeric fraction B2, exhibit no such features (Figure S1). These data demonstrate that the red-shifted spectroscopic signatures arise specifically from the highest-order oligomer, which represents the functional rVCP examined in this study.

The structure of rVCP was determined by cryo-EM as illustrated in Figure 1. The map revealed a tetrameric conformation comprising two dimeric components. Refinement without symmetry (C_1) showed almost no difference between the two dimers. When C_2 symmetry was imposed, a global resolution of 2.42 Å was achieved (Figure S2 and Table S1).

The two monomeric proteins in the rVCP tetramer were identified based on sequence assignment to the cryo-EM map. Monomer-1 and monomer-3 were assigned to DN29098,[21] and monomer-2 and monomer-4 to DN2982,[21] based on distinct differences observed in the cryo-EM map comparisons in the loop regions between transmembrane helices (TMHs) B and C (the BC loop), and between TMHs C and A (the CA loop) (Figure S3a−h and Table S2). For simplicity, we refer to the structurally equivalent pairs as monomer-1/3 and monomer-2/4 throughout the text.

Eleven Chl *a* molecules in each monomer are clearly assigned based on the cryo-EM map (Figure S4a−c). The 11 Chls (602, 603, 604, 609, 610, 611, 612, 613, 621, 622, and 623) are located at the same binding sites between monomer-1/3 and -2/4, whereas monomer-1/3 has one additional Chl molecule at site 624 (Figure 1g−j, Figure S3i and j). Chl numbering in each complex follows that used in the plant LHCII,[22] with four new Chl molecules assigned additional numbers (621−624).

Carotenoids occupying the four binding sites of each monomer were clearly identified from the cryo-EM map (Figure S4d−g). Following previous conventions, we designated the two sites adjacent to TMHs A and B as L1 and L2, the site near TMH A and an amphipathic helix D as V1, and the site adjacent to TMH C as V2 (Figure 1g−j). Each monomer binds four carotenoids with nearly identical orientations (Figure S3k and l), but with different compositions of two types of carotenoids, 3-acetyl vaucheriaxanthin 19′-ester (Vae) and violaxanthin (Vio): a 2:2 ratio in monomer-1/3, and a 1:3 ratio in monomer-2/4 (Figure 1g−j).

The chemical identities of the carotenoids were determined by HPLC coupled with tandem mass spectrometry, revealing the presence of Vae and Vio, with no detectable free vaucheriaxanthin as previously reported.[20] The relative Vae:Vio ratio in the cryo-EM structure (6:10) closely matches the ratio determined by HPLC (6:9) from the same purified rVCP sample (Supporting Information Text 1). In monomer-1/3, two Vae molecules are bound at the L1 and V2 sites, while two Vio molecules occupy the L2 and V1 sites. In monomer-2/4, a single Vae molecule is bound at L1, and three Vio molecules are bound at L2, V1, and V2. HPLC-MS analysis further identified two Vae variants: Vae-8 (with an octanoate group) and Vae-10 (with a decanoate group), in a ratio of 8.4:1 (Supporting Information Text 1). Accordingly, Vae-8 was modeled as the major species. In monomer-1/3, both Vae molecules are confidently assigned as Vae-8, as the cryo-EM map resolves the acyl chain up to the eighth carbon (Figure S4d), and the octanoate group is tightly enclosed by surrounding residues. In contrast, the acyl chain of Vae in monomer-2 extends outward and is less well-defined, suggesting that the L1 site in monomer-2 is the most plausible binding site for the minor Vae-10 variant.

All carotenoid-binding sites are illustrated in detail in Figure S5, with emphasis on hydrogen bond and interacting residues. Furthermore, based on the globular shape of the cryo-EM map and hydrogen bonding networks, 11 and nine water molecules were assigned to the hydrophobic environments of monomer-1/3 and monomer-2/4, respectively.

Protein Factors for Achieving the Distinctive Tetrameric Assembly. rVCP forms a unique asymmetric parallel dimer in which two monomers are arranged almost perfectly parallel with no angular offset. At the monomer-1/monomer-2 interface, key van der Waals (vdW) interactions are observed

https://doi.org/10.1021/jacs.5c17299
J. Am. Chem. Soc. 2025, 147, 47675−47689

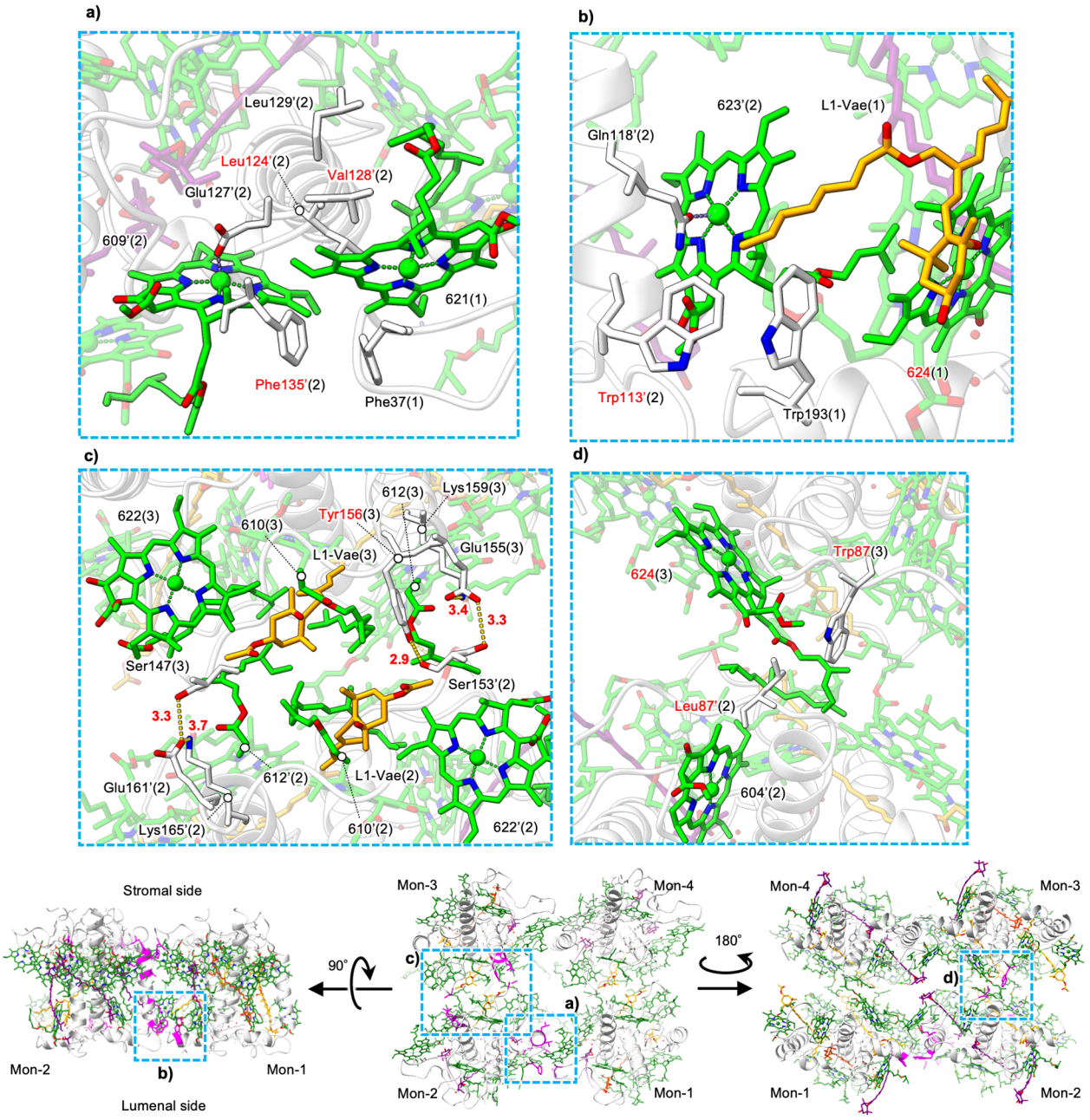

Figure 2. Protein and pigment interactions between monomers for tetramerization. **a, b,** Close-up views of the interface between monomer-1 and monomer-2; **c, d,** close-up views of the interface between monomer-2 and monomer-3. Panels **a** and **c** are viewed from the stromal side; **b** from the membrane plane; and **d** from the lumenal side. The lower panel shows the overall tetramer structure from three different views, with key amino acid residues highlighted in magenta and regions enlarged in **a**–**d** outlined with cyan dashed boxes. Residues are labeled using three-letter codes followed by the monomer number in parentheses (e.g., Trp193(1)). Red labels indicate residues conserved between monomer-1/3 and monomer-2/4.

on both the stromal and lumenal sides. These involve hydrophobic residues such as Phe-37 (N-terminal loop) and Trp-193 (helix D) in monomer-1, and Phe-135′ (CA loop) and Trp-113′ (TMH-C) in monomer-2 (Figure 2a and b). Additional vdW interactions with Chl 621 further stabilize the stromal interface (Figure 2a). Notably, several interface residues in monomer-2 are not conserved in monomer-1 (red labels in Figure 2a and b, Table S2), suggesting an asymmetric organization that gives rise to a distinctive "piggyback" dimer configuration.

Tetramerization involves further interactions between two heterodimers. At the monomer-2/monomer-3 interface, stabilization arises primarily from hydrogen bonds and electrostatic interactions on the stromal side (e.g., Ser-153′–Tyr-156, Glu-155–Ser-153′, and Ser-147–Glu-161′), supported by hydrophobic pigment packings (Figure 2c) and a lumenal vdW contact (Leu-87′–Trp-87) (Figure 2d). Here also several residues are not conserved between monomer-2 and monomer-3 (red labels in Figure 2c,d).

Structural comparison with other LHC oligomers—such as trimeric plant LHCII[22] and tetrameric diatom FCP[25]—highlights the distinctive arrangement of rVCP (Figure 3a–f). While the core helical scaffolds are conserved, rVCP monomers have shorter TMHs and longer N-terminal regions

https://doi.org/10.1021/jacs.5c17299
J. Am. Chem. Soc. 2025, 147, 47675–47689

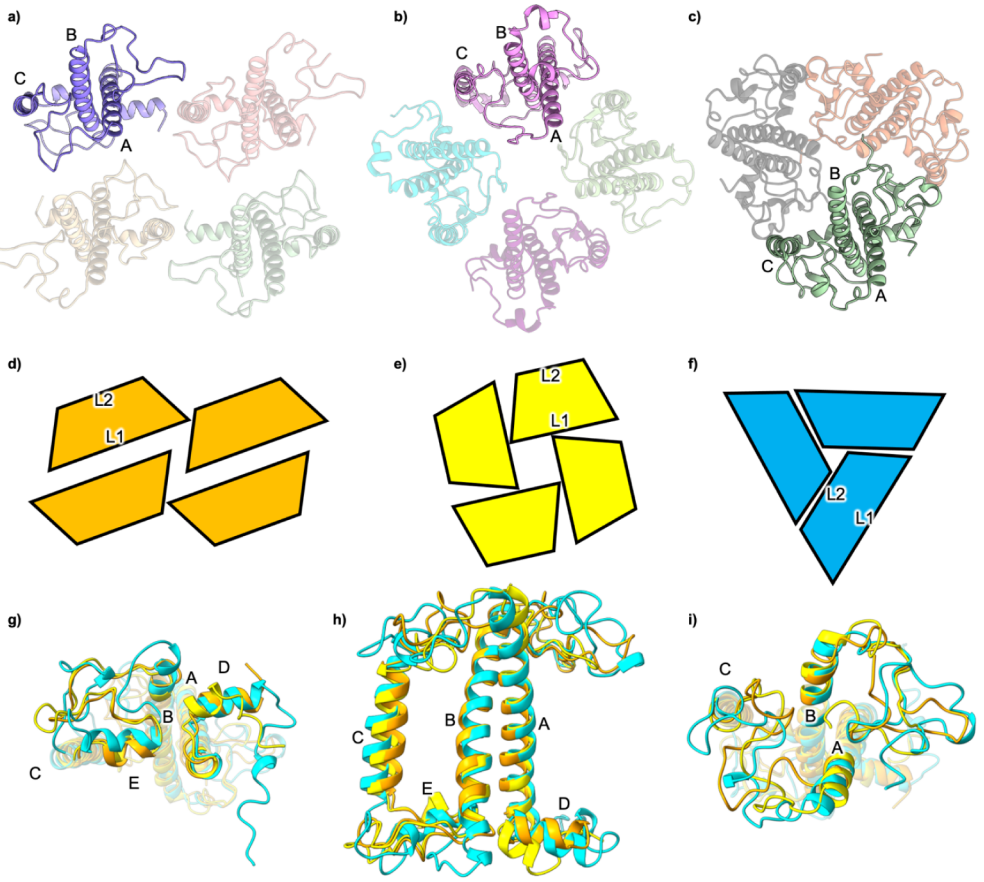

Figure 3. Structural comparison of oligomeric assemblies and monomeric protein conformations among rVCP, *Cg*-FCP, and LHCII. **a**–**c**, Tetrameric assemblies of rVCP (**a**, this work), FCP (**b**, PDB: 8WCK), and trimeric LHCII (**c**, PDB: 1RWT), viewed from the stromal side. **d**–**f**, Schematic representations corresponding to **a**–**c**, illustrating the relative orientation and packing of monomers within each oligomer. **g**–**i**, Superimposition of protein portions of individual monomers from rVCP (orange), FCP (yellow), and LHCII (cyan), viewed from the lumenal (C-terminal) (**g**), lateral (**h**), and stromal (N-terminal) (**i**) sides. Superposition was performed using CCP4MG[63] by aligning the three transmembrane helices. The short and long sides of the trapezoid indicate the directions of the L2 and L1 sites, respectively, serving as orientation markers.

(Figure 3g–i). These features likely contribute to its unique mode of oligomerization. In contrast to the angular offsets seen in Antarctic green algal LHC[27] and plant PSI-LHCI,[28] rVCP dimers maintain a parallel configuration with a longitudinal shift, but no angular rotation between monomers (Figure S6). As a result, the tetramer arranges as a dimer-of-dimers with outward-facing L2 sites, producing a distinct pigment geometry.

Chlorophyll Arrangements for Generating Red-Shifted Absorption. The overall arrangement of Chl molecules in rVCP is distinct from those of other light-harvesting complexes. On the stromal side (Figure 4a), each monomer contains eight Chls, and a total of 32 Chls form densely packed Chl clusters within the tetramer. A key feature is the extension of the putative terminal emitter Chl cluster (610–612–611) by Chl 621, which lies adjacent to Chl 611. This structural proximity supports strong excitonic coupling between Chl 611 and Chl 621 (−180 cm^{-1}) according to quantum chemical calculations (*vide infra*), indicating a robust interaction within each monomer (Table S3 and Supporting Information Text 2). Furthermore, this 610–612–611–621 cluster is connected to an adjacent cluster (609′–603′–602′) via a moderate coupling between Chl 621 and Chl 609′ (73 cm^{-1}), forming an extended intradimer pigment network. This is illustrated in Figure 4e, which provides a close-up of the spatial arrangement of this cluster. Although Chl 622 is spatially near this cluster, its weak coupling with Chl 610 (−2 cm^{-1}) suggests that it is not directly involved in the terminal emitter function. Instead, it exhibits stronger coupling with Chl 609 (−31 cm^{-1}), implying a different role in the pigment network. Collectively, these Chls form a large intradimer cluster: 602′–603′–609′–621–611–612–610. This extended cluster arises from the unique spatial arrangement between monomers in the rVCP tetramer. Additionally, smaller Chl clusters with similar coupling patterns—such as 609–603–602 and 610′–612′–611′–621′—are also observed (Figure 4a, Table S3).

The lumenal side contains fewer Chl molecules per monomer: Chls 604, 613, 623, and 624 in monomer-1/3, and 604′, 613′, and 623′ in monomer-2/4 (Figure 4b). These Chls are spaced more widely than those on the stromal side with distances comparable to those between the stromal and lumenal Chl layers (Figure 4c,d). Excitonic couplings among lumenal Chls are relatively weak (approximately 20–40 cm^{-1}), indicating that no strongly coupled cluster is formed on the lumenal side (Table S3). Notably, the Mg–Mg distance between Chl 624 (lumenal) and Chl 612 (stromal) is only 12.2 Å, which is shorter than any pairwise Chl–Chl distance within the lumenal layer. Their coupling value of 44 cm^{-1} (Figure 4d, Table S3) suggests that Chl 624 may serve as a potential interlayer energy transfer bridge between the lumenal and stromal Chl layers.

https://doi.org/10.1021/jacs.5c17299
J. Am. Chem. Soc. 2025, 147, 47675–47689

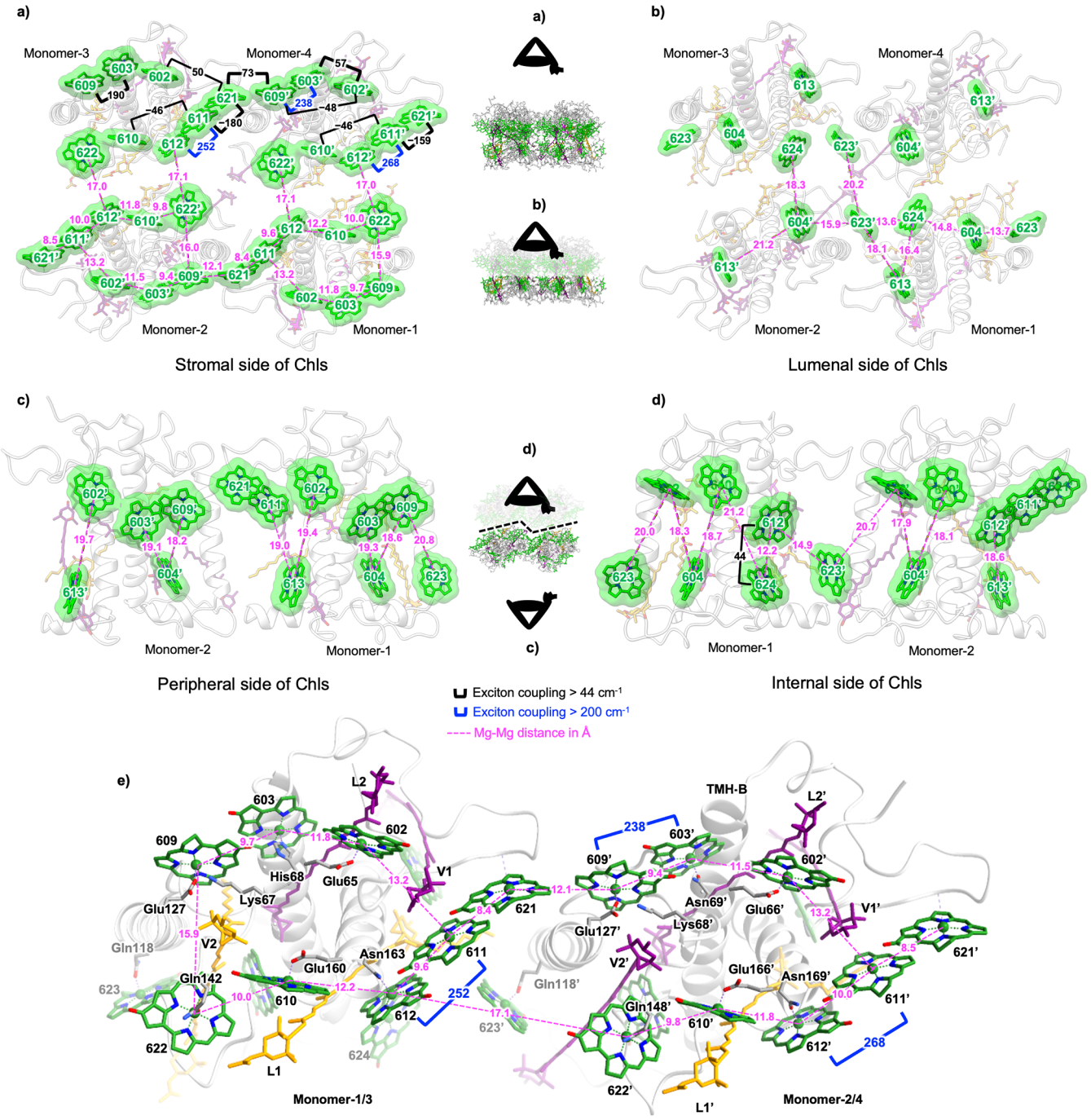

Figure 4. Chlorophyll arrangement, interchlorophyll distances, and excitonic couplings in rVCP. **a, b,** Top views of the tetramer showing the stromal (**a**) and lumenal (**b**) chlorophyll layers, both viewed from the stromal side. **c, d,** Side views of a dimer unit (monomers 1 and 2) viewed from the peripheral side (**c**) and from the dimer−dimer interface (**d**). **e,** Arrangement of pigments and axial ligands in a dimer unit, viewed from the stromal side (corresponding to the region shown in **a**). Magenta numbers indicate the center-to-center distances (Å) between chlorophylls, shown as dotted lines. Black and blue numbers denote calculated excitonic coupling values (cm^{-1}) for Chl−Chl pairs with absolute values >44 cm^{-1} and >200 cm^{-1}, represented by U-shaped connectors in black and blue, respectively. Eye symbols indicate the viewing directions. Chlorophyll side chains have been omitted for clarity.

Origin of the Red-Shifted Chl *a* Absorption. To investigate the origin of far-red Chl *a* absorption in rVCP,[20] we employed quantum chemical calculations based on the cryo-EM structure. Quantum mechanics/molecular mechanics (QM/MM) geometry optimizations and excited-state calculations (see Materials and Methods) were conducted for all Chl pigments, allowing the determination of Chl site energies and Chl−Chl excitonic couplings. These calculations account for the effect of the polarizable protein environment on both the site energies and couplings. Given the symmetry between monomers 1−2 and 3−4, we restrict our discussion to monomers 1 and 2.

The simulated absorption spectrum, resulting from the first-principles excitonic Hamiltonian, showed two peaks of similar intensity separated by ∼25 nm (Figure 5a), closely reproducing the experimentally observed dual-band feature in

https://doi.org/10.1021/jacs.5c17299
J. Am. Chem. Soc. 2025, 147, 47675−47689

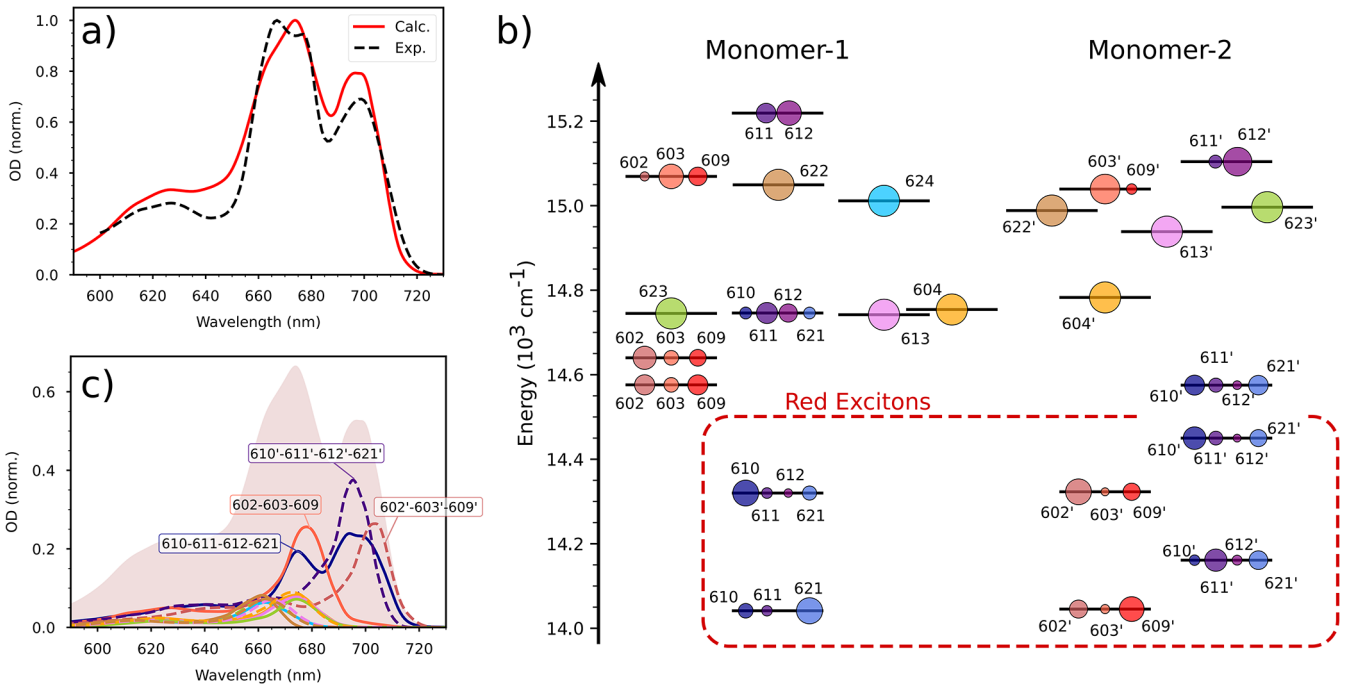

Figure 5. Quantum chemical analysis of excitons in rVCP. **a**, Comparison between the absorption spectrum calculated from first principles and the experimental spectrum measured at 77 K. **b**, Approximate energy levels (zero-phonon lines) and site compositions for Q_y excitons in monomers 1 and 2 of rVCP. Values represent averages over the static disorder. **c**, Contributions of pigment clusters, as defined in **b**, to the overall absorption of rVCP. Clusters in monomers 1 (solid lines) and 2 (dashed lines) are distinguished; unlabeled lines correspond to individual pigments. The shaded red region shows the calculated absorption spectrum from **a**, which is rescaled for visual clarity. All spectra and energies are uniformly shifted by −1800 cm^{-1} to account for systematic errors in the excited-state quantum chemical method.

the Chl Q_y region.[20] An analysis of the energy levels accounting for disorder reveals that the lowest exciton states belong to three pigment clusters: the 610−612−611−621 cluster in monomer-1 plus the 602′−603′−609′ and 610′−612′−611′−621′ clusters of monomer-2 (Figure 5b). The red-shifted band arises almost exclusively from the absorption of these clusters (Figure 5c): Therefore, the far-red band contains contributions from both monomers, with monomer-2 contributing more.

We simulated the spectra at 300 K, assuming that the exciton Hamiltonian remains the same as in cryogenic conditions. The simulated absorption spectrum exhibited two peaks at ∼670 and ∼700 nm, in reasonable agreement with experimental data (Figure S7a), although this time the red band is too red-shifted by ∼5 nm. It is likely that exciton parameters (site energies or couplings) slightly change from cryogenic to room temperatures,[29] following small structural adjustments. The simulated CD spectrum (Figure S7b) qualitatively reproduced the overall positive−negative−negative signal pattern, although the intensities of the negative band at ∼700 nm and the positive band at ∼640 nm are overestimated. Simulating the CD spectrum is challenging due to its high sensitivity to slight pigment orientation changes.[29] Moreover, the nonconservative experimental CD signal in the Q_y region indicates that nonresonant interactions, such as with carotenoid excited states, affect band intensities.[30] In our model, only Q_y transitions are included; thus, the simulated CD spectrum is conservative and overestimates the positive contributions.

The energetic location of exciton states arises from protein-induced modifications to the Chl site energies and delocalization across multiple Chls enabled by excitonic couplings. Our QM/MM calculations indicate that Chls 610 and 621 have red-shifted site energies in both monomers, with additional red-shifted Chls (602′, 609′, and 611′) present in monomer-2 (Figure S8). Some of these Chls exhibit notably large exciton couplings (>200 cm^{-1}) with neighboring Chls, such as 603′−609′ (238 cm^{-1}) and 611′−612′ (268 cm^{-1}) pairs (Figure 4a and e), which results in energy splitting further reducing the energy of low excitons. Furthermore, the red-shifted Chl 621 extends the 610−612−611 domain in both monomers, and participates in the lowest exciton states. Comparison with plant LHCs showed that the 611−612 coupling is over 20% larger than in plant LHCII[31] and the 603−609 coupling is ∼45% larger than in CP29[32] (Table S4), which can be attributed to differences in the arrangement of the Chl pairs (Figure S9).

We remark that our calculations can explain the significantly red-shifted and intense absorption band at 695 nm within the standard exciton model without invoking charge−transfer (CT) states. While CT states are undoubtedly responsible for red-shifted states in the PSI antenna complexes,[14,15,33−35] they are also associated with weak and broad absorption bands, as well as with large Stokes shifts in emission. This is not the case in rVCP, where the red-shifted band is almost as strong as the main band at ∼675 nm, and the fluorescence resembles that of LHCII.[20] Therefore, we assign the red band to strongly delocalized pure excitons in the three terminal emitter domains.

The excitonic character of the terminal emitter in the rVCP is supported by both indirect and direct experimental evidence. Indirect indication was found in the transient absorption spectra associated with red Chl *a*,[20] which exhibited a prominent excited-state absorption band with a characteristic

https://doi.org/10.1021/jacs.5c17299
J. Am. Chem. Soc. 2025, 147, 47675−47689

"wavy" shape—similar to the signals reported for strongly coupled BChl *a* systems in purple bacterial antenna complexes.[36,37] In parallel, our quantum chemical calculation indicated Chl 621 as a contributor to the red-shifted absorption within the 612−611−621 cluster. Agostini et al.[21] constructed a phylogenetic tree of several LHCs and *Nannochloropsis* VCP, which showed that Lhcv1, and Lhcv2 are closely related to the rVCP sequences. The multiple sequence alignment analysis, including both rVCP and VCP sequences (Table S2), revealed that VCP lacks a tryptophan residue in the N-terminal region—the axial ligand at the site corresponding to Chl 621—although other axial ligands are conserved. The axial ligand of Chl 621, the main-chain carbonyl of this tryptophan residue, is unlikely to contribute significantly to spectral tuning. However, a sequence comparison of VCP and rVCP shows that several residues surrounding this site are absent in VCP (Table S2), which may affect the stability of Chl 621. Although the structure of VCP has not been determined, this inference is based on the structural context observed in rVCP. As partly mentioned in Figure 2a and Figure S10k, the carbon atoms of residues surrounding Chl 621, beyond the backbone carbonyl, form a hydrophobic surface (white surfaces in Figure S11) that likely stabilizes Chl 621. Based on this sequence analysis, since VCP lacks these supporting residues, Chl 621 cannot be stably accommodated in VCP. Thus, the sequence difference likely underlies the absence of far-red absorption in VCP and supports the role of Chl 621 in extending the Chl clustering in rVCP.

As direct evidence, we measured the fluorescence quantum yield and lifetime of rVCP, and we derived the dipole strength of its terminal emitter, as described in Supporting Information Text 3. The dipole strength was approximately twice that of isolated Chl *a*, and 1.7-fold larger than that of VCP. This enhancement provides experimental support for the functional role of Chl 621, which is uniquely present in rVCP and facilitates excitonic delocalization across an extended terminal emitter cluster. Together, these findings suggest that the terminal emitter in rVCP incorporates an extended Chl network and that the structural inclusion of Chl 621 contributes directly to the far-red light absorption.

Based on our calculations, the excitonic coupling within the three far-red Chl clusters was notably strong, particularly between Chls 612−611 (252 cm^{-1}), 612′−611′ (268 cm^{-1}), and 603′−609′ (238 cm^{-1}) (Figure 4a and e). What structural features generate such a strong coupling? Agostini et al.[21] proposed that Asn residues play a key role in stabilizing the Chl 603−609 cluster in various LHCs, by forming hydrogen bonds with the 13^1-carbonyl group of Chl 609 and by reducing steric hindrance through small side chains such as Gly or Ala. These features collectively help maintain orbital overlap in the flexible protein environment. In rVCP, all three far-red Chl clusters share a common feature: an Asn residue serves as the axial ligand for Chls 612, 612′, and 603′ (Figure 4e). In each case, the axial Asn ligand also engages in a hydrogen bond-like interactions (∼3.0 Å) with the 13^1-carbonyl group of the adjacent Chl (611, 611′, and 609′, respectively; see Figure S12). In contrast, Chl 603, which is a part of the higher-energy 602−603−609 cluster, is coordinated by His-68 (Figure S12b). At the Chl 603′ site, Gly-65′—located four residues upstream of the axial ligand Asp-69′—is consistent with the proposed A/GxxxN motif that may indicate a red-shifted Chl site. Although Chls 612 and 612′ lack this motif, each is axially ligated by an Asn residue whose side chain interacts with the adjacent Chl—two features consistent with the structural basis for red-shifted absorption proposed by Agostini et al.[21] Together with our coupling calculations, these findings support the role of Asn ligation in promoting tighter pigment packing and stronger excitonic interactions. Consistently, far-red absorbing LHCs such as *Pc*-frLHC and some LHCI exhibit a conserved Asn residue at equivalent axial positions (Table S5). Importantly, among LHCI complexes, only Lhca3 and Lhca4 possess red-shifted Chl *a* pigments and share this Asn feature. Since Lhca3 and Lhca4 have very similar structural and spectroscopic characteristics, hereafter we focus on Lhca4 as a representative red-shifted LHCI protein. Notably, in *Pc*-frLHC, the 603−609 pair exhibits the strongest coupling.[16]

rVCP-Specific Chls 621, 623, and 624 Binding Patterns. In both monomers of rVCP, eight sites (602, 603, 604, 609, 610, 611, 612, and 613) were conserved with the well-studied plant LHCII[22] (Figure S10a−c), while nine slightly different sites (602, 603, 604, 609, 610, 612, 613, and 623) were conserved with the reported tetrameric light-harvesting complex of a diatom *Chaetoceros gracilis*, *Cg*-FCP[25,38] (Figure S13a and b, Table S5). Despite binding different chlorophyll types (Chl *a* and Chl c_2), site 623 in rVCP and site 310 in *Cg*-FCP are both ligated by Gln (Table S5). Residues proximal to the axial ligand are also highly conserved, suggesting structural preservation of this binding site across the two complexes (Figure S13c and d). While Chl 621 appears to occupy a site comparable to Chl *b* 601 in plant LHCII and Chl *a* 301 in red algal Lhcr1, its angular orientations and precise positioning differ markedly from those counterparts (Figure S10 a, b, d, and e). Notably, the binding orientation of Chl 601 in CP29 is nearly identical with that in LHCII. Based on these comparisons, Chls 621, 622, and 624 appear to represent rVCP-specific binding sites.

The primary structural differences between the corresponding sites—621 in rVCP and 601 in LHCII—lie in the identity of the axial ligand coordinated to Chl 611, which is adjacent to each site, and in the shape of the binding cavity, which is influenced by differences in N-terminal residues. The axial ligand of Chl 611 in LHCII is phosphatidylglycerol (PG) (Figure S10l), while that of rVCP is a water molecule. The absence of the PG molecule provides room for the Chl 621 to be inserted in rVCP and form a well-coupled cluster with Chl 611 (Figure S10k and l). Additionally, the binding of Chl 621 is stabilized by a hydrogen-bonding network including the 3-hydroxyl group of V1-Vio, and the 13^1-carbonyl group of Chl 621 via a water molecule of an axial ligand of Chl 611. Note that Chl 621 and Chl 611 exhibit strong $\pi-\pi$ stacking between the C and A rings, respectively, resulting in a short Mg−Mg distance of 8.4 Å. Furthermore, the Trp-36 residue, the axial ligand of Chl 621, constitutes part of a hydrophobic wall formed with Phe-37 and other hydrophobic residues (*vide supra*), which stabilize Chl 621 (Figure 2a, Figures S10k and S11). These amino acid positions allow for the formation of a unique arrangement between Chls 621 and 611.

A comparison of Chl arrangements between the two monomers revealed differences at sites 623/623′ and 624 (Figure S14). Chl 623 and 623′ are both axially ligated by Gln, yet Chl 623′ shows a notable tilt (Figure S14a). The binding environment at Chl 623 involves Leu-114 and Gly-115, whereas at the Chl 623′ site, these residues are replaced by Ala-114′ and Val-115′, respectively (Figure S14b and c). These replacements effectively swap the steric bulkiness at the two

https://doi.org/10.1021/jacs.5c17299
J. Am. Chem. Soc. 2025, 147, 47675−47689

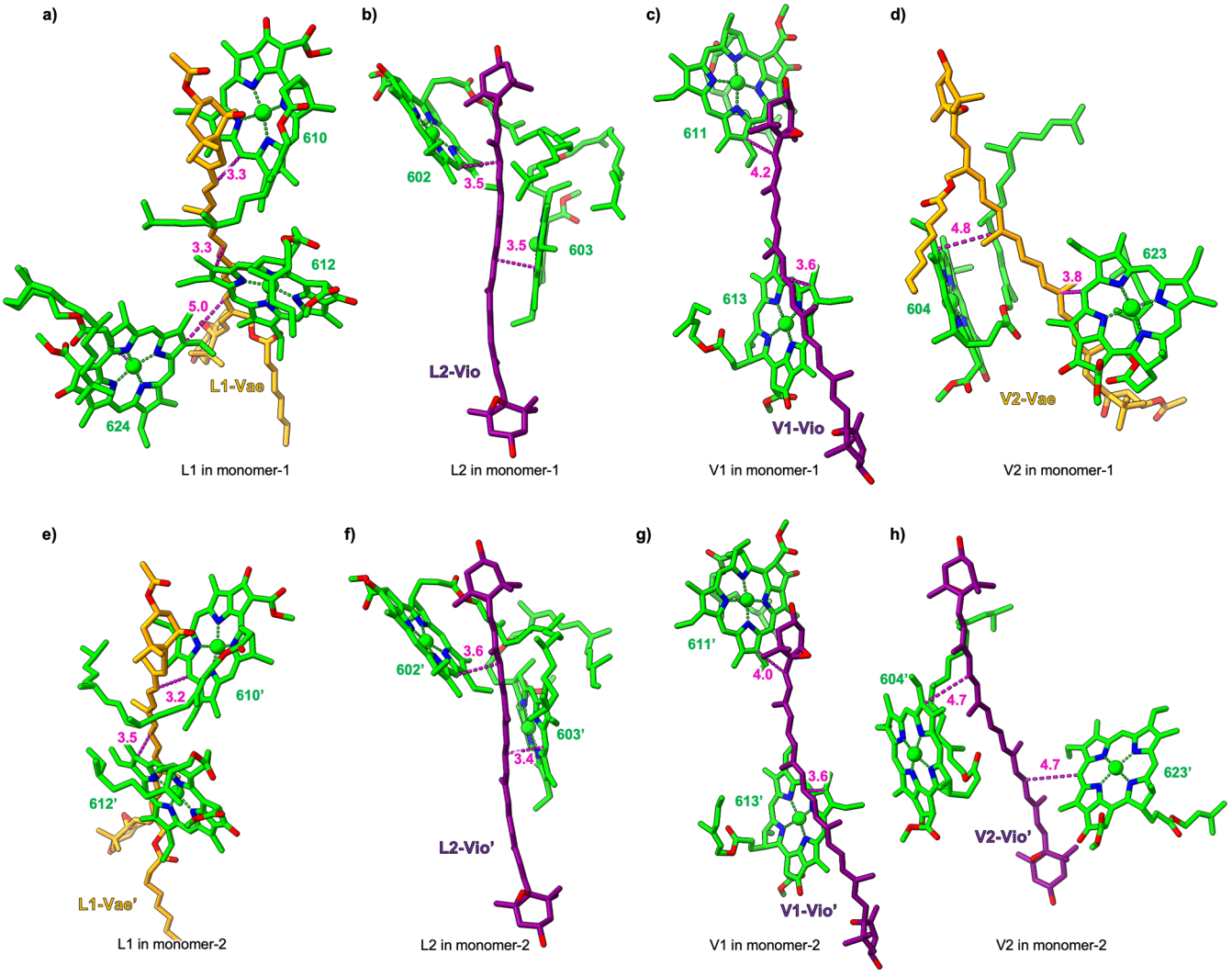

Figure 6. Carotenoid−chlorophyll clusters in the rVCP structure. Carotenoid−chlorophyll clusters at the L1, L2, V1, and V2 sites are shown for monomer-1 (**a**−**d**) and monomer-2 (**e**−**h**), respectively. Red numbers indicate distances (in Å) corresponding to the dotted lines.

positions, resulting in marked differences in the binding geometry of Chl 623/623′. Site 624 is unique to monomer-1 (Figure S3i). Chl 624 is axially coordinated by a water molecule hydrogen bonded to the main-chain carbonyls of Thr-83 and Phe-80 (Figure S14d). The macrocycle of Chl 624 is stabilized by $\pi-\pi$ stacking between its A-ring and Phe-80, which is conserved in both monomers. Additionally, monomer-1-specific residues Trp-87 and Ile-187 form a hydrophobic pocket that further stabilizes Chl 624 binding.

Carotenoid Binding Sites, Chl-Carotenoid Clusters. The carotenoid binding orientations in rVCP are more similar to those in *Cg*-FCP and Lhcr1 than to those in LHCII (Figure S13e−j). Among the four binding sites in rVCP, the L1 and L2 sites are highly conserved across LHCs from various species, including FCP, Lhcr1, and LHCII. In contrast, the V1 and V2 sites in rVCP differ significantly from those in LHCII (Figure S13i and j), but closely resemble their counterparts in *Cg*-FCP and Lhcr1 (Figure S13e−h). These differences include subtle variations in the orientation of the ionone end rings and the distortion pattern of the conjugation chain. A comparison between the two monomers of rVCP revealed that the V2 site exhibits distinct distortion patterns, whereas the other three sites showed little monomer-dependent variation in distortion pattern (Figure S3k and l).

The Chl-carotenoid clusters differ between the two monomers. The L1−610−612 cluster and L2−602−603 cluster in both monomers resemble those in plant LHCII with similar short $\pi-\pi$ distances (3.4 to 3.6 Å) and spatial arrangements (Figure 6a, b, e, and f). However, in monomer-1, the L1 cluster also includes Chl 624 at a distance of 3.9 Å (Figure 6a). At the V1 sites of both monomers, $\pi-\pi$ distances of 3.6 Å support the formation of the V1-Vio−Chl 613 cluster (Figure 6c and g). In contrast, in the V2 site shows marked differences between monomers. In monomer-1, Chl 623 is closely aligned with Vae (3.8 Å) with parallel conjugated systems, indicating strong coupling (Figure 6d). But in monomer-2, Chl 623′ is tilted (Figure S14a) and more distant from Vio (Figure 6h), suggesting significantly weaker energetic coupling.

Chl−Car and Chl−Chl Energy Transfer. Efficient triplet−triplet energy transfer between red-shifted Chls and carotenoids has been identified in rVCP,[21] which suggests that vdW contacts exist between the triplet-quenching carotenoid and the red-shifted Chl molecule. Based on our far-red Chls assignments, we propose the L1-Vae−Chl 612, L1-Vae′−Chl

https://doi.org/10.1021/jacs.5c17299
J. Am. Chem. Soc. 2025, 147, 47675−47689

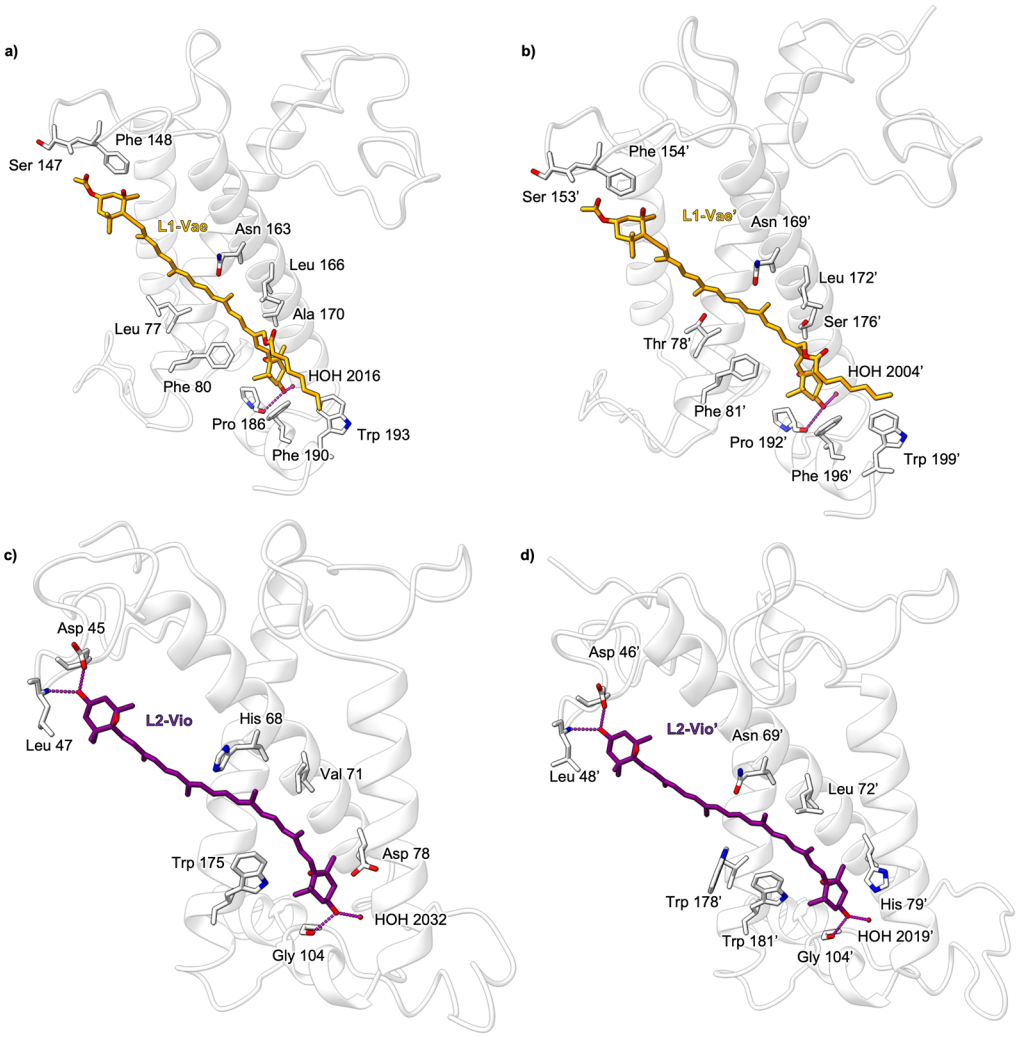

Figure 7. Characteristics of carotenoid-binding sites potentially contributing to red-shifted absorption. Specific amino acid residues in the L1 (**a** and **b**) and L2 (**c** and **d**) binding sites of monomer-1 and -2, respectively, that may contribute to the red-shift of carotenoid absorption are highlighted.

612′, and L2-Vio′−Chl 603′ domains as candidate triplet−triplet quenching sites. Ultrafast spectroscopy also shows that singlet energy transfer occurs primarily via the carotenoid S_2 state to Chls that are not excitonically coupled, with red Chls populated through subsequent energy transfer within the Chl pool.[20] Based on our structure, Chls 604 and 623 in both monomers are likely S_2-mediated singlet energy acceptors (∼100 fs) from V2-site carotenoids (Vae in monomer-1 or Vio in monomer-2), while Chl 613 appears to accept energy from V1-site Vio in both monomers (Figure 6c,d). Additionally, carotenoids bound at the L1 and L2 sites likely contribute to slower (ps-scale) energy transfer via the carotenoid S_1 state.

Spectroscopically, two distinct carotenoid pools absorbing at ∼490 and ∼510 nm have been reported.[20] Based on the 3D structure of rVCP, specific carotenoids can be tentatively assigned to each spectral component. Bína et al.[20] also indicated that all carotenoids in the 510 nm pool and a portion of those in the 490 nm pool are directly associated with the red-shifted Chls. Given that only the carotenoids at the L1 and L2 sites are in direct vdW contact with far-red Chls in our structure, these sites likely correspond to the 510 and 490 nm pools. Despite chemical differences between Vio and Vae (Figure S4), their effective conjugation lengths are similar;[39,40] the observed spectral variation likely arises from interactions with specific amino acid residues. The binding pockets of the L1 and L2 sites differ subtly between the two monomers (Figure 7). For example, the environment around L1-Vae in monomer-1 is more hydrophobic (Ala-170 and Leu-77) than in monomer-2 (Ser-176′ and Thr-78′). The L2 pocket shows more pronounced differences: in monomer-1, His-68 (potentially positively charged) is present near the center of the conjugated chain and Asp-78 at the end-group toward the lumen, while these are replaced by Asn-69′ and His-79′, respectively, in monomer-2. These charged and polar substitutions could modulate carotenoid excited-state properties.[41−43] Given the minor contribution of the 510 nm carotenoid pool to the absorption spectrum of rVCP, it is likely that one or two L2 carotenoids are responsible for this pool.

Finally, owing to its high site energy among lumenal Chls (Figure 5b), Chl 624 may not serve efficiently as an intermediate for energy transfer, even though its spatial arrangement suggests a potential energy-hub role binding stromal and lumenal Chl layers (Figure 4b and d). Given that the energy gap between Chl 624 and other lumenal Chls (604, 604′, 613, 613′, 623, and 623′) is approximately 300 cm^{-1}

https://doi.org/10.1021/jacs.5c17299
J. Am. Chem. Soc. 2025, 147, 47675−47689

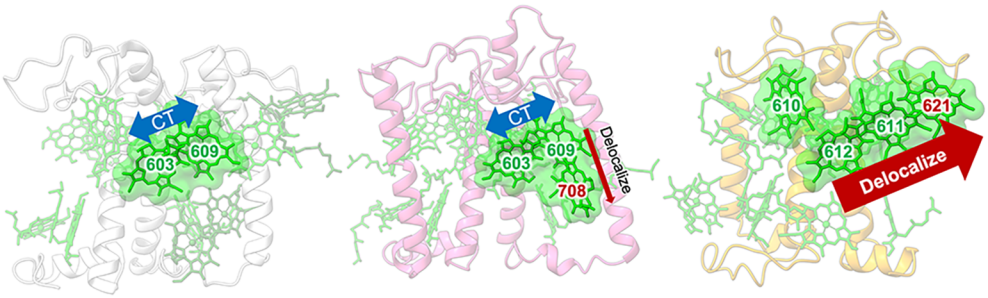

		Lhca4	Pc-frLHC	rVCP (This work)
Mechanism	CT	○*1	○*2	–
	Delocalization	–	△*2	◎*3
Method	QM/MM	○*1	○*2	○*3
	Experiments	○*4		
Structure	Axial ligand	Asn*5	Asn*6	Asn*3
Energy at 77 K (Wavelength)	Red-absorption	>700 nm*7	~708 nm*6	~695 nm*8
	Emission	~733 nm*6	~730 nm*6	~712 nm*8

Figure 8. Conceptual overview and comparative data summary of far-red absorption mechanisms in three Chl *a*-based photosynthetic complexes. Representative models (top) illustrate three types of far-red absorption: CT-only (Lhca4, PDB ID 7DKZ, left), CT−delocalization hybrid (*Pc*-frLHC, PDB ID 8HW1, center), and delocalization-only (this work, right). The table (bottom) summarizes key features, including the contributions of each mechanism (○: present, ◎: strong, –: absent), the axial ligands of red-shifted chlorophyll *a*, and the observed energies at 77 K. *[1]refs [Sláma et al.[15], Rankelytė et al.[34]]; *[2]ref [Saito et al.[16]]; *[3]This work; *[4]refs [Romero et al.[14], Wientjes et al.[33]]; *[5]ref [Wang et al.[28]]; *[6]ref [Kosugi et al.[27]]; *[7]ref [Morosinotto et al.[35]]; *[8]ref [Bína et al.[20]].

(Figure S8), uphill energy transfer seems plausible in rVCP, as seen in other far-red absorbing systems.[27,44,45] Given that the excitonic couplings between stromal and lumenal Chl pairs are generally weaker (Figure 4c and d), Chl 624 may function as an energy hub, bridging the stromal and lumenal Chl layers.

Unique Strategy for Far-Red Absorption Compared with the Other Far-Red Absorbing LHCs. Until now, three Chl *a*-based far-red absorbing LHCs have been structurally and computationally characterized: Lhca4, *Pc*-frLHC, and rVCP (Figure 8). All three utilize exclusively Chl *a* to generate far-red excitation energy, exhibiting absorption and fluorescence peaks near 700 and ∼710−730 nm, respectively. Structurally, they share two key features: Asn residues serving as axial ligands to red-form Chls, and well-conserved dimeric or trimeric Chl clusters on the stromal side that provide the basis for far-red tuning. In Lhca4, both quantum chemical calculations[15,34] and spectroscopic studies[14,33,46] suggest that far-red absorption primarily arises from charge−transfer (CT) interactions within the 603−609 pigment pair. *Pc*-frLHC retains this CT mechanism but additionally incorporates Chl 708, which expands the excitonic cluster and enhances delocalization over the 603−609 pair. In contrast, rVCP adopts a fundamentally different strategy. It achieves far-red absorption solely through excitonic delocalization without involving any CT contributions. This unique mechanism is driven by the incorporation of Chl 621 into the terminal emitter cluster (610−612−611), offering a distinct structural principle for red-shifting light absorption in LHCs. Together, these findings position rVCP as the first structurally characterized LHC that achieves far-red Chl *a* absorption through pure excitonic delocalization, in contrast to CT-based or hybrid CT-delocalized mechanisms observed in other LHCs.

Red-shifted absorption achieved purely through excitonic delocalization offers a key advantage over CT-mediated mechanisms. CT-induced red shifts are inherently unstable: CT character decays exponentially with pigment−pigment distance, making these states extremely sensitive to slight structural fluctuations.[36] In contrast, excitonic delocalization remains rather insensitive to such structural variations and maintains strongly allowed far-red absorption, providing a more robust basis for energy transfer. In our system, the tetrameric rVCP, containing two well-conserved chlorophyll clusters connected via Chl 621 in each dimeric unit, represents a structurally stable platform that supports far-red utilization via excitonic delocalization. These features suggest that exploiting excitonic mechanisms rather than CT states could serve as a general design principle for engineering light-harvesting complexes with improved robustness and enhanced potential for crop or algal productivity.

■ CONCLUSION

In this study, we determined the high-resolution cryo-EM structure of rVCP from *Trachydiscus minutus*, a member of the Eustigmatophyceae (a class of algae). The structure reveals that rVCP adopts a heterodimer-based tetrameric architecture, a configuration not previously reported for LHCs. It features a distinctive Chl *a* arrangement, including the incorporation of Chl 621, which underlies the structural basis for far-red absorption in LHCs containing only Chl *a* pigments. Moreover, quantum chemical calculations revealed that the far-red exciton arises purely from excitonic delocalization, enabled by the extended Chl cluster formed through this distinctive pigment arrangement. This mechanism contrasts with those of previously characterized far-red absorbing LHCs, which rely on charge−transfer interactions. Comparative analysis of these differences among far-red absorbing LHCs advances our understanding of the mechanisms responsible for far-red absorption in these systems. Such insights position rVCP as a key model system for the further exploration of delocalization-driven red shifts.

https://doi.org/10.1021/jacs.5c17299
J. Am. Chem. Soc. 2025, 147, 47675−47689

MATERIALS AND METHODS

Sample Preparations. Samples of rVCP were prepared from cells of *Trachydiscus minutus*, strain CCALA 931, as described previously.[10,20] Briefly, cells were batch-cultured in 5 L Erlenmeyer flasks in a freshwater WC medium at 20 °C. Halogen light bulbs were used to illuminate the cultures with red-enhanced light. Thylakoid proteins were purified from thylakoid membranes solubilized with *n*-Dodecyl β-D-maltoside (β-DDM) by sucrose gradient ultracentrifugation (0.1−1.1 M, 100,000 × *g*, 17 h). The sucrose gradient fraction corresponding to the highest oligomeric state of rVCP (corresponding to B5 in ref 10) was then washed with a sucrose-free buffer. The detergent in the micellar rVCP complex was exchanged from β-DDM to Lauryl Maltose Neopentyl Glycol (LMNG) using ultrafiltration (AmiconUltra-0.5, 100 kDa) by alternating three times additions of a buffer (25 mM HEPES-NaOH at pH 7.5) and the buffer containing 0.5% (w/v) LMNG. The sample was repurified using sucrose density ultracentrifugation (P55ST2 rotor, Hitachi, 50,000 rpm, 5 h, 4 °C), with a stepwise layering of 0.2−0.5 and 1.0 M sucrose in buffer solution (50 mM MES, 10 mM NaCl, 20 mM $CaCl_2$, 0.002% LMNG). The tetrameric rVCP band was collected, and the sucrose in the solution was eliminated through ultrafiltration using AmiconUltra-0.5 (100 kDa) with a 25 mM HEPES-NaOH buffer (pH 7.5) containing 0.002% LMNG.

Cryo-EM Data Collection. We used the multiple blotting method[47] with modifications to overcome low sample concentration. Quantifoil Cu R 1.2/1.3 holey carbon grids on both sides were performed by hydrophilic treatment using JEC-3000RC (JEOL, Japan), for 10 s at 10 mA. A 2.5 μL aliquot of two types of rVCP (∼5.0 mg mL^{-1}) was applied to both sides of the grid and then manually blotted at room temperature. Quickly moving on to the normal blotting operation, 2.5 μL of the sample was applied on the grid and frozen in liquid ethane using the Vitrobot IV system (FEI) at 4 °C, 100% humidity, 3 s blotting time, 5 s waiting time, and blotting force −10. Data for rVCP were collected on a CRYO ARM 300 (CryoJEM-Z300FSC, JEOL, Japan), respectively, equipped with a cold field-emission electron detector camera (Gatan, USA). The Cryo-EM images were collected using Serial-EM.[48] The holes were detected using YoneoLocker.[49] Movie frames were recorded using a K3 camera at a nominal magnification of ×60,000 corresponding to pixel sizes of 0.873 Å (CRYO ARM 300 II) at the specimen level. The data were collected with a total exposure of 3 s fractionated into 40 frames, with a total of ∼80 electrons $Å^{-2}$ in counting mode. The movies were collected with defocus values varying from 0.7 to 2.2 μm. Typical cryo-EM images averaged from motion-corrected movie frames are shown in Figure S2.

Cryo-EM Data Processing. A gain reference image was prepared with the relion_estimate_gain command in RELION 4.0[50] using the first 300 movies. Images were processed using cryoSPARC ver. 4.2.1.[51] A total of 9,306 and 7,135 movies of rVCP were imported and motion corrected, and contrast transfer functions (CTFs) were estimated. A total of 6,350 and 6,116 movies with maximum CTF resolutions greater than 5 Å were selected. The particles were automatically picked using a template picker job with a particle diameter at 250 Å using templates made from the cryo-EM map of rVCP prepared in advance. After particle extraction with 2× binning, two-dimensional (2D) classification into 50 classes was performed to select clear 2D class averages. Additionally, several rounds of 2D classifications with various conditions were performed, and Ab initio reconstructions were performed using selected 398,806 particles, resulting in five maps (Class 0 to 4). Three maps (Class 0, 2, 4) were selected, and total particles (316,992) were extracted again with a box size of 0.873 pixels without binning and were subjected to the round of homogeneous refinement. After the global and local CTF refinements and nonuniform refinement, heterogeneous refinement was performed using the refined map and two maps from contaminant classes in the Ab initio reconstruction (Class 1 and 3). Two rounds of local, global, and nonuniform refinements were applied to the extracted 290,174 particles. Finally, the additional two rounds of local, global, and nonuniform refinements were performed with imposing C_2 symmetry. A final map was reconstructed at 2.42 Å resolution (FSC = 0.143). The processing strategy is detailed in Figure S2.

Model Building and Validation. The atomic models of rVCP were constructed using WinCOOT 0.9.447,[52] Phenix 1.19-41584,[53] and both Chimera and ChimeraX[54] software packages. The coordinate of LHCII (PDB: 1RWT) was directly docked as a template into the cryo-EM map of rVCP using Chimera such that the transmembrane helices were roughly matched to the cryo-EM map. The sequence was replaced by DN29098 and DN2982.[21] The coordinate of Vae (vaucheriaxanthin 3-acetate 19′-octanoate, Code: A1L1F) was newly made based on the ChemDraw structure by Global Phasing Limited, grade2 (https://grade.globalphasing.org/cgi-bin/grade2_server.cgi). The geometry-optimized model was globally refined in Phenix to achieve a global resolution of each electron potential map. The refinement statistics are summarized in Table S1.

Quantum Chemical Calculations. We performed molecular mechanics (MM) and hybrid quantum mechanics/molecular mechanics (QM/MM) optimizations for the rVCP structure in the present work (see Supporting Information Text 2 for details). An MM minimization with strong restraints (4 kcal $mol^{-1}Å^{-2}$) on the protein backbone and Chl rings was followed by QM/MM geometry optimizations of each Chl ring at the B3LYP/6-31G(d) level with a frozen MM environment. We verified that the optimized structure of rVCP was still compatible with the cryo-EM map. On the rVCP structure thus refined, we performed polarizable QM/MM (QM/MMPol) excited-state TD-DFT calculations to obtain Q_y excitation energies and transition properties for all the Chls. In QM/MMPol, each environment atom is endowed with a polarizability in addition to a point charge.[55−57] Excited-state calculations were performed with the M06-2X functional,[58] which has proven effective for Chl *a* in LHCs.[30−32] Exciton couplings were computed analytically as the Coulomb interaction between transition densities of the interacting states, and including the explicit screening effect of the polarizable environment.[59] In all QM/MM(Pol) calculations, the phytol tail of each Chl was included in the MM environment, along with the protein, other cofactors, and water molecules. An exciton Hamiltonian was built considering all Q_y states of all the Chls in the tetramer. This Hamiltonian was used to simulate the absorption and CD spectra of rVCP employing the full second-order cumulant expansion approach (FCE).[29,60] This approach accounts for nonsecular and non-Markovian effects in the line shape. Inhomogeneous broadening was accounted for by random shifts of the site energies

https://doi.org/10.1021/jacs.5c17299
J. Am. Chem. Soc. 2025, 147, 47675−47689

extracted from independent Gaussian distributions. We used the spectral density for Chl *a* extracted from experiments on LHCII.[61] All quantum chemical calculations were performed with a locally modified version of the Gaussian16 package. Spectra were simulated using the pyQME program (https://github.com/Molecolab-Pisa/pyQME doi: 10.1063/5.0170295). The analysis of disordered exciton levels was conducted as described in Betti et al.[62]

■ ASSOCIATED CONTENT

Data Availability Statement

Coordinate data for the structure of rVCP have been deposited in the PDB under accession code 9MCC. The Cryo-EM map with C_2 symmetry has been deposited in the Electron Microscopy Data Bank under accession code EMD-63799.

Supporting Information

The Supporting Information is available free of charge at https://pubs.acs.org/doi/10.1021/jacs.5c17299.

Comparison of steady-state spectroscopy of rVCP and its smaller form, a putative monomer, Cryo-EM data processing procedure, Comparison of proteins and pigments between monomer-1 and -2: identification of amino acid sequences based on the cryo-EM map, Chemical structure of each pigment with the corresponding cryo-EM map, Differences in carotenoid-binding pockets in rVCP, Oligomeric structural comparison among rVCP, *Pt*-FCP dimer, *Pc*-frLHC undecamer, and LHCI associated with PSI, Comparison of simulated and experimental spectra at room temperature, Site energies of Chls in rVCP, Comparison of rVCP terminal emitter domains with plant PSII antennas, Superposition structure focusing on Chl 612−611 cluster among rVCP, LHCII, Lhcr1, *Pc*-frLHC, and Lhca4, Binding sites of Chl 621 in monomer-1/3 and Chl 621′ in monomer-2/4, Axial ligands and hydrogen bonding residues of Chls, Superposition structure between rVCP and FCP and carotenoids structural comparison among rVCP, *Cg*-FCP, Lhcr1, and LHCII, Comparison of the Chl binding sites 623 and 624 between the two monomers, Cryo-EM data collection, refinement and validation statistics, Sequential comparison of *Trachydiscus minutes* rVCP proteins (monomer 1/3 and monomer 2/4) and *Nannochloropsis oceanica* putative VCP proteins (Lhcv1 and Lhcv2), Excitonic couplings (in cm^{-1}) between Chls within adjacent monomers of rVCP, Main exciton couplings (in cm^{-1}) in Chl pairs and comparison with equivalent couplings in LHCII/CP29, The lists of axial ligands of each monomer in rVCP with plant LHCII, CP29, Lhca3, and Lhca4, green alga *Prasiola crispa* (*Pc*)-frLHC and diatom *Chaetoceros gracilis* (*Cg*)-FCP, Pigment composition of rVCP and identification of acylated vaucheriaxanthin peaks, Computational details for MM and QM/MM refinement, Comparison of the dipole strengths, Supplementary References (PDF)

■ AUTHOR INFORMATION

Corresponding Authors

Soichiro Seki − *Graduate School of Science, Osaka City University, Osaka 558-8585, Japan; Institute for Protein Research, The University of Osaka, Suita, Osaka 565-0871, Japan*; Email: s-seki@protein.osaka-u.ac.jp

Radek Litvín − *University of South Bohemia in České Budějovice, Faculty of Science, České Budějovice 370 05, Czech Republic; Czech Academy of Sciences, Biology Centre, Institute of Plant Molecular Biology, České Budějovice 370 05, Czech Republic*; orcid.org/0000-0001-5272-9029; Email: rlitvin@prf.jcu.cz

Ritsuko Fujii − *Graduate School of Science, Osaka City University, Osaka 558-8585, Japan; Graduate School of Science and Research Center for Artificial Photosynthesis, Osaka Metropolitan University, Osaka 558-8585, Japan*; orcid.org/0000-0003-1492-109X; Email: ritsuko@omu.ac.jp

Authors

Lorenzo Cupellini − *Dipartimento di Chimica e Chimica Industriale, University of Pisa, Pisa 56124, Italy*; orcid.org/0000-0003-0848-2908

David Bína − *University of South Bohemia in České Budějovice, Faculty of Science, České Budějovice 370 05, Czech Republic; Czech Academy of Sciences, Biology Centre, Institute of Plant Molecular Biology, České Budějovice 370 05, Czech Republic*

Elena Betti − *Dipartimento di Chimica e Chimica Industriale, University of Pisa, Pisa 56124, Italy*; orcid.org/0009-0005-5204-3680

Petra Urajová − *Centre Algatech, Institute of Microbiology, Czech Academy of Sciences, Třeboň 379 01, Czech Republic*

Hideaki Tanaka − *Institute for Protein Research, The University of Osaka, Suita, Osaka 565-0871, Japan*

Tomoko Miyata − *Graduate School of Frontier Biosciences and JEOL YOKOGUSHI Research Alliance Laboratories, The University of Osaka, Suita, Osaka 565-0871, Japan*

Keiichi Namba − *Graduate School of Frontier Biosciences and JEOL YOKOGUSHI Research Alliance Laboratories, The University of Osaka, Suita, Osaka 565-0871, Japan*

Genji Kurisu − *Institute for Protein Research, The University of Osaka, Suita, Osaka 565-0871, Japan; JEOL YOKOGUSHI Research Alliance Laboratories and Institute for Open and Transdisciplinary Research Initiatives, The University of Osaka, Suita, Osaka 565-0871, Japan*

Tomáš Polívka − *University of South Bohemia in České Budějovice, Faculty of Science, České Budějovice 370 05, Czech Republic*

Complete contact information is available at: https://pubs.acs.org/10.1021/jacs.5c17299

Notes

The authors declare no competing financial interest.

■ ACKNOWLEDGMENTS

This work was supported by JSPS KAKENHI Grant Number 24H02091 (to R.F.); JSPS KAKENHI Grant Number 25K18413 and Grant-in-aid for JSPS Fellowships Grant Number 23KJ1834 and 25KJ0223 (to S.S.); JSPS KAKENHI Grant Number 23H04958 and JST CREST Grant Number JPMJCR20E1 (to G.K.); the Platform Project for Supporting Drug Discovery and Life Science Research (BINDS) from AMED under Grant Number JP23ama121001 (to G.K.) and JP23ama121003 (to K.N.); and JEOL YOKOGUSHI Research Alliance Laboratories of Osaka University (to K.N.). Work in the Czech Republic was supported by OP JAK project Photomachines reg. no. CZ.02.01.01/00/22_008/0004624

(to D.B., P.U., T.P., and R.L.), D.B. and R.L. also acknowledge institutional support RVO: 60077344.

REFERENCES

(1) Iwai, M.; Patel-Tupper, D.; Niyogi, K. K. Structural Diversity in Eukaryotic Photosynthetic Light Harvesting. *Annu. Rev. Plant. Biol.* **2024**, *75* (1), 119−152.
(2) Nicol, L.; Croce, R.; van Grondelle, R.; van Amerongen, H.; van Stokkum, I. Light Harvesting in Higher Plants and Green Algae. In *Light harvesting in photosynthesis*; CRC Press, 2018, pp. 59−76. DOI: .
(3) Croce, R.; van Amerongen, H. Light harvesting in oxygenic photosynthesis: Structural biology meets spectroscopy. *Science* **2020**, *369* (6506), No. eaay2058.
(4) Collini, E. Carotenoids in Photosynthesis: The Revenge of the "Accessory" Pigments. *Chem* **2019**, *5*, 494−495.
(5) Stomp, M.; Huisman, J.; Stal, L.; et al. Colorful niches of phototrophic microorganisms shaped by vibrations of the water molecule. *ISME J.* **2007**, *1*, 271−282.
(6) Wolf, B. M.; Blankenship, R. E. Far-red light acclimation in diverse oxygenic photosynthetic organisms. *Photosynth. Res.* **2019**, *142*, 349−359.
(7) Gisriel, C. J. Recent structural discoveries of photosystems I and II acclimated to absorb far-red light. *Biochim. Biophys. Acta, Bioenerg.* **2024**, *1865*, 149032.
(8) Croce, R.; van Amerongen, H. Light-harvesting in photosystem I. *Photosynth. Res.* **2013**, *116*, 153−166.
(9) Herbstová, M.; Bína, D.; Koník, P.; Gardian, Z.; Vácha, F.; Litvín, R. Molecular basis of chromatic adaptation in pennate diatom *Phaeodactylum tricornutum*. *Biochim. Biophys. Acta* **2015**, *1847* (6−7), 534−543.
(10) Litvín, R.; Bína, D.; Herbstová, M.; Pazderník, M.; Kotabová, E.; Gardian, Z.; Trtílek, M.; Prášil, O.; Vácha, F. Red-shifted light-harvesting system of freshwater eukaryotic alga *Trachydiscus minutus* (Eustigmatophyta, Stramenopila). *Photosynth. Res.* **2019**, *142* (2), 137−151.
(11) Chen, M.; Blankenship, R. E. Expanding the solar spectrum used by photosynthesis. *Trends Plant Sci.* **2011**, *16* (8), 427−431.
(12) Ort, D. R.; et al. Redesigning photosynthesis to sustainably meet global food and bioenergy demand. *Proc. Natl. Acad. Sci. U. S. A.* **2015**, *112*, 8529−8536.
(13) Walter, J.; Kromdijk, J. Here comes the sun: How optimization of photosynthetic light reactions can boost crop yields. *J. Integr. Plant Biol.* **2022**, *64*, 564−591.
(14) Romero, E.; Mozzo, M.; van Stokkum, I. H.; Dekker, J. P.; van Grondelle, R.; Croce, R. The origin of the low-energy form of photosystem I light-harvesting complex Lhca4: mixing of the lowest exciton with a charge-transfer state. *Biophys. J.* **2009**, *96* (5), L35−7.
(15) Sláma, V.; Cupellini, L.; Mascoli, V.; Liguori, N.; Croce, R.; Mennucci, B. Origin of Low-Lying Red States in the Lhca4 Light-Harvesting Complex of Photosystem I. *J. Phys. Chem. Lett.* **2023**, *14* (37), 8345−8352.
(16) Saito, K.; Kosugi, M.; Qiu, L.; Minagawa, J.; Ishikita, H. Identification and design principles of far-red-absorbing chlorophyll in the light-harvesting complex. *J. Biol. Chem.* **2025**, *301* (6), 108518.
(17) Maistro, S.; Broady, P.; Andreoli, C.; Negrisolo, E. Xanthophyceae. In *Handbook of the Protists*; Archibald, J., et al., Ed.; Springer: Cham, 2016. DOI: .
(18) Llansola-Portoles, M. J.; Litvín, R.; Ilioaia, C.; Pascal, A. A.; Bína, D.; Robert, B. Pigment structure in the violaxanthin−chlorophyll-*a*-binding protein VCP. *Photosynth. Res.* **2017**, *134*, 51−58.
(19) Keşan, G.; Litvín, R.; Bína, D.; Durchan, M.; Šlouf, V.; Polívka, T. Efficient light-harvesting using non-carbonyl carotenoids: Energy transfer dynamics in the VCP complex from *Nannochloropsis oceanica*. *Biochim. Biophys. Acta, Bioenerg.* **2016**, *1857*, 370−379.
(20) Bína, D.; Durchan, M.; Kuznetsova, V.; Vácha, F.; Litvín, R.; Polívka, T. Energy transfer dynamics in a red-shifted violaxanthin-chlorophyll *a* light-harvesting complex. *Biochim. Biophys. Acta, Bioenerg.* **2019**, *1860*, 111−120.
(21) Agostini, A.; Bína, D.; Barcytė, D.; Bortolus, M.; Eliáš, M.; Carbonera, D.; Litvín, R. Eustigmatophyte model of red-shifted chlorophyll *a* absorption in light-harvesting complexes. *Commun. Biol.* **2024**, *7*, 1406.
(22) Liu, Z.; et al. Crystal Structure of Spinach Major Light-Harvesting Complex at 2.72 Å Resolution. *Nature* **2004**, *18*, 287−292.
(23) Standfuss, J.; Van Scheltinga, A. C. T.; Lamborghini, M.; Kühlbrandt, W. Mechanisms of photoprotection and nonphotochemical quenching in pea light-harvesting complex at 2.5 Å resolution. *EMBO J.* **2005**, *24* (5), 919−928.
(24) Wang, W.; et al. Structural basis for blue-green light harvesting and energy dissipation in diatoms. *Science* **2019**, *363* (6427), No. eaav0365.
(25) Zhou, C.; et al. Structural and spectroscopic insights into fucoxanthin chlorophyll a/c-binding proteins of diatoms in diverse oligomeric states. *Plant Commun.* **2024**, *5* (11), 101041.
(26) La Rocca, R.; Kato, K.; Tsai, P. C.; et al. Structure of a photosystem II-FCPII supercomplex from a haptophyte reveals a distinct antenna organization. *Nat. Commun.* **2025**, *16*, 4175.
(27) Kosugi, M.; Kawasaki, M.; Shibata, Y.; Hara, K.; Takaichi, S.; Moriya, T.; Adachi, N.; Kamei, Y.; Kashino, Y.; Kudoh, S.; Koike, H.; Senda, T. Uphill energy transfer mechanism for photosynthesis in an Antarctic alga. *Nat. Commun.* **2023**, *14*, 730.
(28) Wang, J.; Yu, L. J.; Wang, W.; Yan, Q.; Kuang, T.; Qin, X.; Shen, J. R. Structure of plant photosystem I-light harvesting complex I supercomplex at 2.4 angstrom resolution. *J. Integr. Plant Biol.* **2021**, *63*, 1367−1381.
(29) Cupellini, L.; Lipparini, F.; Cao, J. Absorption and circular dichroism spectra of molecular aggregates with the full cumulant expansion. *J. Phys. Chem. B* **2020**, *124* (39), 8610−8617.
(30) Prandi, I. G.; Sláma, V.; Pecorilla, C.; et al. Structure of the stress-related LHCSR1 complex determined by an integrated computational strategy. *Commun. Biol.* **2022**, *5* (1), 145.
(31) Sláma, V.; Cupellini, L.; Mennucci, B. Exciton properties and optical spectra of light harvesting complex II from a fully atomistic description. *Phys. Chem. Chem. Phys.* **2020**, *22*, 16783−16795.
(32) Saraceno, P.; Sardar, S.; Caferri, R.; Camargo, F. V. A.; Dall'osto, L.; D'Andrea, C.; Bassi, R.; Cupellini, L.; Cerullo, G.; Mennucci, B. Probing the Effect of Mutations on Light Harvesting in CP29 by Transient Absorption and First-Principles Simulations. *J. Phys. Chem. Lett.* **2024**, *15* (24), 6398−6408.
(33) Wientjes, E.; Roest, G.; Croce, R. From red to blue to far-red in Lhca4: How does the protein modulate the spectral properties of the pigments? *Biochim. Biophys. Acta, Bioenerg.* **2012**, *1817*, 711−717.
(34) Rankelytė, G.; Gelzinis, A.; Robert, B.; Valkunas, L.; Chmeliov, J. Environment-dependent chlorophyll−chlorophyll charge transfer states in Lhca4 pigment−protein complex. *Front. Plant Sci.* **2024**, *15*, 1412750.
(35) Morosinotto, T.; Mozzo, M.; Bassi, R.; Croce, R. Pigment-Pigment Interactions in Lhca4 Antenna Complex of Higher Plants Photosystem I. *J. Biol. Chem.* **2005**, *280*, 20612−20619.
(36) Cupellini, L.; Caprasecca, S.; Guido, C. A.; Müh, F.; Renger, T.; Mennucci, B. Coupling to Charge Transfer States is the Key to Modulate the Optical Bands for Efficient Light Harvesting in Purple Bacteria. *J. Phys. Chem. Lett.* **2018**, *9* (23), 6892−6899.
(37) Kennis, J. T.; Streltsov, A. M.; Vulto, S. I.; Aartsma, T. J.; Nozawa, T.; Amesz, J. Femtosecond dynamics in isolated LH2 complexes of various species of purple bacteria. *J. Phys. Chem. B* **1997**, *101* (39), 7827−7834.
(38) Nagao, R.; Kato, K.; Kumazawa, M.; Ifuku, K.; Yokono, M.; Suzuki, T.; Dohmae, N.; Akita, F.; Akimoto, S.; Miyazaki, N.; Shen, J. R. Structural basis for different types of hetero-tetrameric light-harvesting complexes in a diatom PSII-FCPII supercomplex. *Nat. Commun.* **2022**, *13*, 1764.
(39) Polivka, T.; Sundström, V. Ultrafast Dynamics of Carotenoid Excited States-From Solution to Natural and Artificial Systems. *Chem. Rev.* **2004**, *104* (4), 2021−2072.
(40) Macernis, M.; Streckaite, S.; Litvin, R.; Pascal, A. A.; Llansola-Portoles, M. J.; Robert, B.; Valkunas, L. Electronic and Vibrational

Properties of Allene Carotenoids. *J. Phys. Chem. A* **2022**, *126*, 813−824.
(41) Schulte, T.; et al. Identification of a single peridinin sensing Chl-a excitation in reconstituted PCP by crystallography and spectroscopy. *Proc. Natl. Acad. Sci. U. S. A.* **2009**, *106*, 20764−20769.
(42) Sauer, V.; Cupellini, L.; Sutter, M.; Bondanza, M.; Domínguez Martin, M. A.; Kirst, H.; Bína, D.; Koh, A. F.; Kotecha, A.; Greber, B. J.; Nogales, E.; Polívka, T.; Mennucci, B.; Kerfeld, C. A. Structural and Quantum Chemical Basis for OCP-Mediated Quenching of Phycobilisomes. *Sci. Adv.* **2024**, *10* (14), No. eadk7535.
(43) Fujimoto, K. J.; Seki, T.; Minoda, T.; Yanai, T. Spectral Tuning and Excitation-Energy Transfer by Unique Carotenoids in Diatom Light-Harvesting Antenna. *J. Am. Chem. Soc.* **2024**, *146*, 3984−3991.
(44) Pettai, H.; Oja, V.; Freiberg, A.; Laisk, A. Photosynthetic Activity of Far-Red Light in Green Plants. *Biochim. Biophys. Acta Bioenerg.* **2005**, *1708* (3), 311−321.
(45) Elias, E.; Brache, K.; Schäfers, J.; Croce, R. Coloring Outside the Lines: Exploiting Pigment−Protein Synergy for Far-Red Absorption in Plant Light-Harvesting Complexes. *J. Am. Chem. Soc.* **2024**, *146* (5), 3508−3520.
(46) Croce, R.; Chojnicka, A.; Morosinotto, T.; Ihalainen, J. A.; van Mourik, F.; et al. The Low-Energy Forms of Photosystem I Light-Harvesting Complexes: Spectroscopic Properties and Pigment-Pigment Interaction Characteristics. *Biophys. J.* **2007**, *93*, 2418−2428.
(47) Mastronarde, D. N. Automated electron microscope tomography using robust prediction of specimen movements. *J. Struct. Biol.* **2005**, *152*, 36−51.
(48) Snijder, J.; Borst, A. J.; Dosey, A.; Walls, A. C.; Burrell, A.; Reddy, V. S.; Kollman, J. M.; Veesler, D. Vitrification after multiple rounds of sample application and blotting improves particle density on cryo-electron microscopy grids. *J. Struct. Biol.* **2017**, *198*, 38−42.
(49) Yonekura, K.; Maki-Yonekura, S.; Naitow, H.; Hamaguchi, T.; Takaba, K. Machine learning-based real-time object locator/evaluator for cryo-EM data collection. *Commun. Biol.* **2021**, *4*, 1044.
(50) Zivanov, J.; Nakane, T.; Forsberg, B. O.; Kimanius, D.; Hagen, W. J. H.; Lindahl, E.; Scheres, S. H. W. New tools for automated high-resolution cryo-EM structure determination in RELION-3. *eLife* **2018**, *7*, No. e42166.
(51) Punjani, A.; Rubinstein, J. L.; Fleet, D. J.; Brubaker, M. A. CryoSPARC: Algorithms for rapid unsupervised cryo-EM structure determination. *Nat. Methods* **2017**, *14*, 290−296.
(52) Emsley, P.; Lohkamp, B.; Scott, W. G.; Cowtan, K. Features and development of Coot. *Acta Crystallogr. D Biol. Crystallogr.* **2010**, *66*, 486−501.
(53) Adams, P. D.; et al. PHENIX: A comprehensive Python-based system for macromolecular structure solution. *Acta Crystallogr. D Biol. Crystallogr.* **2010**, *66*, 213−221.
(54) Pettersen, E. F.; Goddard, T. D.; Huang, C. C.; Couch, G. S.; Greenblatt, M.; Meng, E. C.; Ferrin, T. E. UCSF Chimera - A visualization system for exploratory research and analysis. *J. Comput. Chem.* **2004**, *25* (13), 1605−1612.
(55) Bondanza, M.; Nottoli, M.; Cupellini, L.; Lipparini, F.; Mennucci, B. Polarizable Embedding QM/MM: The Future Gold Standard for Complex (Bio)Systems? *Phys. Chem. Chem. Phys.* **2020**, *22*, 14433−14448.
(56) Nottoli, M.; Cupellini, L.; Lipparini, F.; Granucci, G.; Mennucci, B. Multiscale Models for Light-Driven Processes. *Annu. Rev. Phys. Chem.* **2021**, *72*, 489−513.
(57) Lipparini, F. General Linear Scaling Implementation of Polarizable Embedding Schemes. *J. Chem. Theory Comput.* **2019**, *15* (8), 4312−4317.
(58) Zhao, Y.; Truhlar, D. G. The M06 Suite of Density Functionals for Main Group Thermochemistry, Thermochemical Kinetics, Noncovalent Interactions, Excited States, and Transition Elements: Two New Functionals and Systematic Testing of Four M06-Class Functionals and 12 Other Functionals. *Theor. Chem. Acc.* **2008**, *120*, 215−241.
(59) Cupellini, L.; Corbella, M.; Mennucci, B.; Curutchet, C. Electronic Energy Transfer in Biomacromolecules. *WIREs Comput. Mol. Sci.* **2019**, *9*, No. e1392.
(60) Ma, J.; Cao, J. Förster Resonance Energy Transfer, Absorption and Emission Spectra in Multichromophoric Systems. I. Full Cumulant Expansions and System-Bath Entanglement. *J. Chem. Phys.* **2015**, *142* (9), 094106.
(61) Novoderezhkin, V. I.; Palacios, M. A.; van Amerongen, H.; van Grondelle, R. Energy-Transfer Dynamics in the LHCII Complex of Higher Plants: Modified Redfield Approach. *J. Phys. Chem. B* **2004**, *108* (29), 10363−10375.
(62) Betti, E.; Saraceno, P.; Cignoni, E.; Cupellini, L.; Mennucci, B. Insights into Energy Transfer in Light-Harvesting Complex II Through Machine-Learning Assisted Simulations. *J. Phys. Chem. B* **2024**, *128* (21), 5188−5200.
(63) McNicholas, S.; Potterton, E.; Wilson, K. S.; Noble, M. E. M. Presenting Your Structures: The CCP4mg Molecular-Graphics Software. *Acta Crystallogr. D Biol. Crystallogr.* **2011**, *67*, 386−394.

https://doi.org/10.1021/jacs.5c17299
J. Am. Chem. Soc. 2025, 147, 47675−47689